Journal of Materials Chemistry C

Thienoacene dimers based on the thieno[3,2-b]thiophene moiety: Synthesis, Characterization and Electronic Properties

Journal:	*Journal of Materials Chemistry C*
Manuscript ID:	TC-ART-09-2014-002158.R1
Article Type:	Paper
Date Submitted by the Author:	27-Oct-2014
Complete List of Authors:	Geerts, Yves; Université Libre de Bruxelles, Chemistry Niebel, Claude; Ecole Nationale Supérieure de Chimie de Montpellier, Kim, Yeongin; Stanford University, Ruzié, Christian; Université Libre de Bruxelles (ULB), Karpinska, Jolanta; Université Libre de Bruxelles (ULB), Chattopadhyay, Basab; Université Libre de Bruxelles (ULB), Schweicher, Guillaume; Université Libre de Bruxelles (ULB), Richard, Audrey; Université Libre de Bruxelles (ULB), Lemaur, Vincent; Université de Mons, Olivier, Yoann; Université de Mons, Cornil, Jérôme; Université de Mons, Kennedy, A R; University of Strathclyde, Dept. of Pure and Applied Chemistry Diao, Ying; Stanford University, Lee, Wen-Ya; Stanford University, Mannsfeld, Stefan; Center for Advancing Electronics Dresden, Technische Universität Dresden, Bao, Zhenan; Lucent Technologies, Bell Labs

Cite this: DOI: 10.1039/c0xx00000x

www.rsc.org/xxxxxx

ARTICLE TYPE

Thienoacene dimers based on the thieno[3,2-*b*]thiophene moiety: Synthesis, Characterization and Electronic Properties

Claude Niebel, [a,§] Yeongin Kim,[b,§] Christian Ruzié,[a] Jolanta Karpinska,[a] Basab Chattopadhyay,[a] Guillaume Schweicher,[a] Audrey Richard,[a] Vincent Lemaur,[d] Yoann Olivier,[d] Jérôme Cornil,[d] Alan R. Kennedy,[e] Ying Diao,[c] Wen-Ya Lee,[c] Stefan Mannsfeld,[f] Zhenan Bao,[c] and Yves H. Geerts*[a]

Received (in XXX, XXX) Xth XXXXXXXXX 20XX, Accepted Xth XXXXXXXXX 20XX

DOI: 10.1039/b000000x

Two thienoacene dimers based on the thieno[3,2-*b*]thiophene moiety were efficiently synthesized, characterized and evaluated as active hole-transporting layers in organic thin-film field-effect transistors. Both compounds behaved as active p-channel organic semi-conductors showing averaged hole mobility of up to 1.33 $cm^2 V^{-1} s^{-1}$.

Introduction

The demand for high-performance organic field effect transistors has led to an intensive investigation of tailor-made organic semiconductors.[1-3] Among the most efficient organic semi-conductors, thienoacene-based derivatives are of particular interest showing high mobilities coupled with an excellent air stability.[4] Indeed, thienoacene derivatives present a highly delocalized electronic structure and low-lying highest occupied molecular orbital (HOMO) energy level, contributing to outstanding charge transport and air stability. In addition, the strong nonbonded S--S and π--π intermolecular interactions in the solid state promote large intermolecular orbital overlap in this family of semiconductors.[5] These features explain their potentially high charge carrier mobility. In particular, [1]benzothieno[3,2-*b*][1]benzothiophene (BTBT) **1a**, depicted in Figure 1, has been the core of numerous derivatization[6-9] mainly driven towards the discovery of the best p-channel organic semi-conductor.[10,3, 11-13] Takimiya and co-workers have for instance studied the effect of the length of alkyl side chains in a series of 2,7-alkylated BTBT derivatives on the electronic properties of their respective solution processed thin films.[12] The 2,7-dioctyl BTBT **1b** presents an interesting compromise of good solubility in chloroform coupled with a high μ_{FET} over 1 $cm^2 V^{-1} s^{-1}$ and I_{on}/I_{off} of 10^7.[12] Moreover, the extension of the π-conjugation in this type of thienoacene is generally accepted as a mean of enhancing of their charge carrier mobility. Two complementary approaches can be considered for the elaboration of highly extended thienoacenes: the fused approach, which consists of increasing the number of π-units by linking one unit to another one so that they are sharing one C=C double bond; and the oligomer approach, which aims at extending the thienoacene core through the formation of a C-C bond between two adjacent π-units.[14] Mori et al.[15] have recently reported an efficient thiophene-annulation approach for the preparation of two fused π-extended BTBT derivatives (BBTBDT **2** and BBTNDT **3**) that exhibit appreciable mobility values of 10^{-2}-10^{-1} and 5 $cm^2 V^{-1} s^{-1}$, respectively.[13,15] As far as the π-extended oligomeric approach of **1a** is considered, the BTBT dimer **4a** has been mentioned in a Japanese patent without any details upon its synthesis.[16] The compound **4a** has recently been reported by another group while we were preparing our manuscript. **4a** has been synthesized through a different route than ours.[17] We report here the synthesis of the thienoacene dimers **4a,b** from readily available BTBT **1a**. Both dimers were characterized and evaluated as active hole transporting layers in organic thin-film field-effect transistors. The two BTBT dimers appeared as highly efficient p-channel semi-conductors with averaged hole mobilities up to 1.33 $cm^2 V^{-1} s^{-1}$. Dioctyl substituted dimer, **4b** showed improved electronic properties as compared to **4a**.

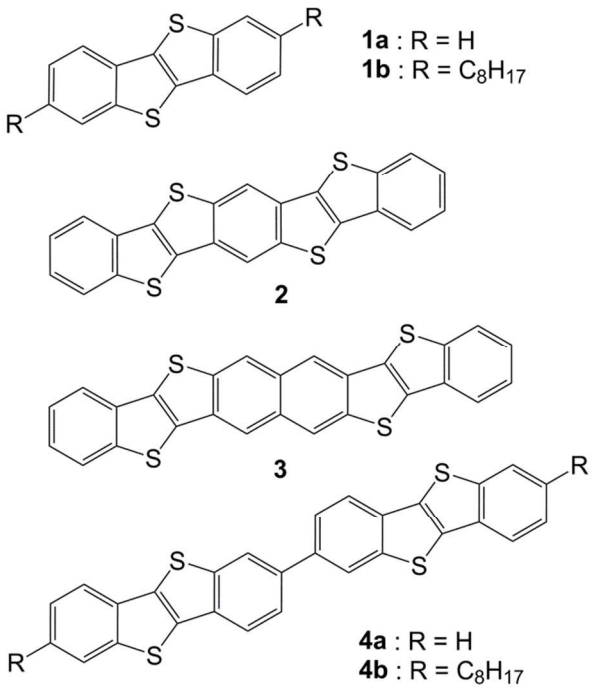

Fig. 1 Molecular structures of benzothiophene derivatives

Results and discussion

Synthesis and characterization

The two thienoacene dimers **4a,b** were prepared following two synthetic procedures depicted on Scheme 1. Both procedures involved the functionalization of the starting [1]benzothieno[3,2-*b*]benzothiophene derivative **1a**, which was easily produced in large scale from commercially available 2-chlorobenzaldehyde and sodium hydrosulfide hydrate.[18] The synthesis of the dimer **4a** involved a first mono nitration of the benzothiophene **1a**, accomplished as described by Svoboda et al[6] by reaction of nitric acid at low temperature. The nitro derivative **5** was then reduced to the primary amine **6**[6] by reaction with iron and ammonium chloride in toluene. Subsequent diazonium formation with sodium nitrite followed by a Sandmeyer reaction with copper (I) bromide afforded 2-bromo-[1]benzothieno[3,2-b][1]benzothiophene (**7**).

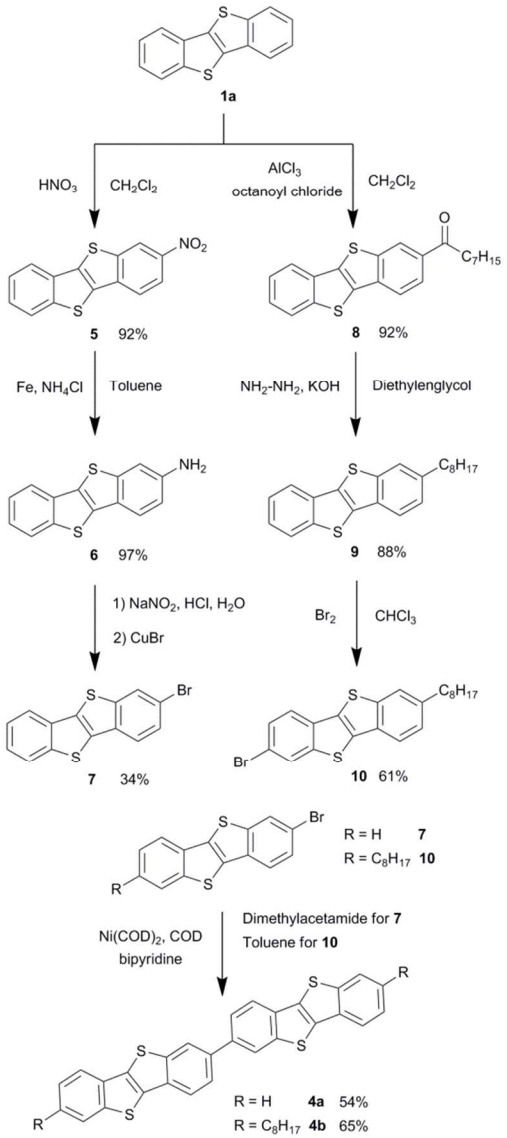

Scheme 1 Synthesis of thienoacene dimers **4a** and **4b**.

A Yamamoto coupling using pure **7** as halide reagent gave the desired dimers **4a** in 54% yield. As expected, **4a** is poorly soluble in common organic solvents and required the use of higher boiling solvents such as chlorobenzene to form homogenous solutions. The synthesis of the dialkylated dimers **4b** started with the preparation of the mono-ketone **8** through a Friedel and Crafts acylation using $AlCl_3$ as Lewis acid.[7, 19, 20] It is worth noting that the temperature should be kept at -78°C during all the reaction to prevent the formation of any polyacylated side product. The octyl-BTBT **9** was then obtained in good yield through a conventional Wolff-Kishner reduction of **8**. The synthesis of the mono-bromo derivative **10** was not as straightforward and required the slow addition of a quasi-stoechiometric amount of bromine to a solution of **9** in chloroform, cooled to 0°C. Indeed, a fast addition of bromine or an increase of the reaction temperature engendered the formation of brominated side products difficult to remove. As previously, a Yamamoto coupling afforded the target dialkylated BTBT dimer **4b** from its bromo precursor **10** in an acceptable yield of 65%. Starting from **1**, the overall yield of **4a,b** reached 16% and 32%, respectively.

The target dimer **4a** was too unsoluble to be characterized by ^{1}H NMR, even in chlorinated solvents at high temperature. However, we managed to record a ^{1}H NMR spectrum of **4b** in deuterated tetrachlorethane at 100°C (see Figure S9). The poor solubility prevented to record a ^{13}C NMR spectrum. MALDI-HRMS corroborates the structure of **4a,b** (see Figures S12 and S13). UV-vis spectra of solutions of **4a,b** exhibit a maximum of absorption at longest wavelength (λ_{max} ABS) at 336 and 358 nm, respectively (Figure S14). The large difference of λ_{max} ABS is attributed to the torsion angle between BTBT units rather than to an electron donating effect of the octyl side chains. A shoulder around 350 nm is apparent for **4a**. The results are corroborated by the maximum of emission at shortest wavelength (λ_{max} EM) that differs only by 4 nm compared to λ_{max} ABS (see Figures S14 and S16).

Single-crystal structure Analysis

Nice plate like single crystals were obtained by liquid/liquid diffusion technique using tetrahydrofuran (THF) and methanol (CH_3OH) for **1a** while crystals of **4a** were grown in a tube-based

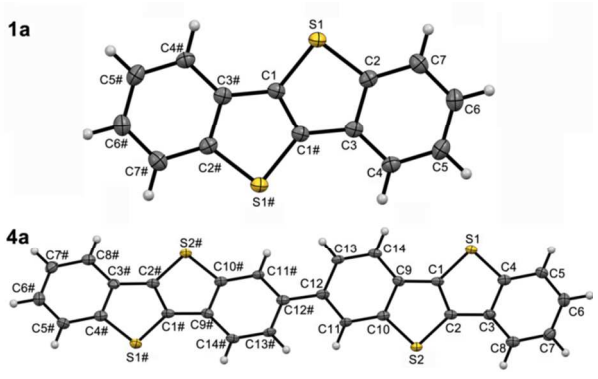

Fig 2. Molecular view of **1a** and **4a**. The atoms marked with # are generated by symmetry.

vacuum sublimation unit. One end of the glass tube containing compound **4a** was placed inside the horizontal furnace (set to 260 °C) while the other end of the glass tube was kept at room temperature (RT). This setup provided a temperature gradient along the condensation zone. Although the synthesis of BTBT (**1a**) has been reported previously[18] surprisingly there is no report of its crystal structure. The knowledge of its crystal structure is essential to understand the effect of different substituents onto the BTBT backbone. Compound **4b** is not soluble at RT, therefore all crystallization experiments were carried out above 80 °C. Despite the use of wide range of organic solvents and different crystallization techniques such as slow evaporation, slow cooling from a single and mixture of solvents as well as liquid and vapour diffusion, we were unable to produce single crystals of **4b** suitable for structure determination. Molecular views of the compounds **1a** and **4a** are given in Figure 1. Compound **1a** crystallizes in a monoclinic unit cell with space group P21/c while Compound **4a** crystallizes in the orthorhombic Pbcn space group; the asymmetric unit of both compounds consists of half of the molecule, i.e. Z′= 0.5. In **4a**, the planar BTBT cores are twisted with respect to each other; the dihedral angle between the two symmetry related cores is 50.26°. This is often found in other structures containing biphenyl motifs and it is also close to the calculated value of twist angle for biphenyl in the gas phase[21]. The crystal structure of **1a** and **4a** can be best described as a "layer by layer" organization with the molecules in each layer packed in a herringbone motif. The herringbone packing has been reported for several other BTBT derivatives like **2**, **3**, and **9**[12,13,15,22]. In **1a** and **4a**, the 2-dimensional herringbone motif is stabilized by C-H…π interactions (Figure 3) as has been observed in the case of **3** and **9**.

Table 1 Crystal data for compound **1a** and **4a**.

	1a	**4a**
Empirical formula	$C_{14}H_8S_2$	$C_{28}H_{14}S_4$
Formula weight	240.32	478.63
Temperature, K	123(2)	123(2)
Wavelength, Å	1.54180	1.54180
Crystal system	Monoclinic	Orthorhombic
Space group	$P2_1/c$	Pbcn
a, b, c(Å)	11.8095(7), 5.8538(3), 7.9599(5)	6.0452(5), 7.7010(7), 43.405(5) Å
α,β,γ (°)	90.0, 105.990(6), 90.0	90.0, 90.0, 90.0
Volume	528.98(5)	2020.7(3) $Å^3$
Z, Z′	2, 0.5	4, 0.5
Density (calculated), Mg/m^3	1.509	1.573
Crystal size (mm^3)	0.38 x 0.25 x 0.04	0.30 x 0.18 x 0.02
Reflections collected	1722	8025
Independent reflections	1022 [R(int) = 0.0227]	1904 [R(int) = 0.1010]
Goodness-of-fit on F^2	1.035	1.105
Final R indices [I>2sigma(I)]	R1 = 0.0439, wR2 = 0.1191	R1 = 0.0762, wR2 = 0.2156
R indices (all data)	R1 = 0.0467, wR2 = 0.1244	R1 = 0.0856, wR2 = 0.2296

Although similar, the crystal structure in **2** is stabilized by π…π interactions forming parallel π-stacked columns interacting with each other only via van der Waals interactions. In the case of dimer **4a** the crystal packing can be visualized as two antiparallel herringbone sheets linked by the bridging C-atoms (Figure 3). In order to have a clear quantitative and visual insight of the intermolecular interactions, the Hirshfeld surfaces of **1a**, **2**, **3**, and

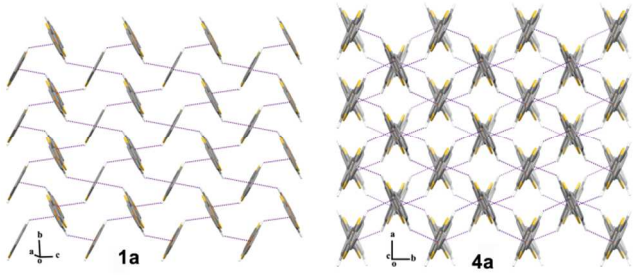

Fig 3. The 2-dimensional herringbone network formed by C-H…π interactions in **1a** and **4a**. The bridged BTBT cores of **4a** are shown in a lighter shade.

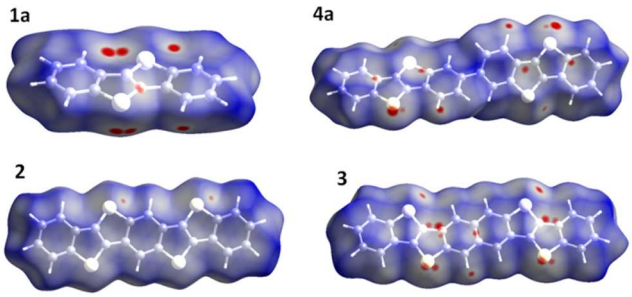

Fig 4. Hirshfeld surfaces for compounds **1a**, **2**, **3** and **4a** mapped over a d_{norm} range of -0.5 to 1.15Å.

4a have been calculated and are presented in Figure 4, showing surfaces that have been mapped over a d_{norm} range of -0.5 to 1.15Å. This allows for a rational understanding of the subtleties of crystal packing arising as a result of dimerization (as in **4a**) and ring-fusion (as in **2** and **3**). The dominant interactions can be seen in the Hirshfeld surfaces (Figure 4) as the bright red areas corresponding to the C-H···π interactions in **1a**, **3** and **4a**, and H···S contacts in **2**. A look at the 2D fingerprint plots (Figure 5) clearly reveals that the packing environments are completely different although all compounds exhibit a similar herringbone motif. The plots of **1a** and **4a** are somewhat similar but with much higher concentration of points for **4a**. The C-H···π hydrogen bonds**,** appear as two pairs of wings of almost equal lengths (d_i, d_e) regions of (1.6 Å, 1.1 Å) and (1.1 Å, 1.6 Å), in Figure 5. In case of **2**, the pair of wings appearing at (d_i, d_e) regions of (1.8 Å, 1.1 Å) and (1.1 Å, 1.8 Å) is a manifestation of short S···H contacts (Figure 5). The higher contribution of π···π interactions in **2** is evident from the higher density of points in the regions d_i= d_e = 2.0 Å (Figure 5). The relative contributions of H···H, S/C···H and C/S···C/S interactions to the Hirshfeld surface area are depicted in Figure 5 for all compounds. The quantitative analysis clearly shows that C···H contacts corresponding to C-H···π interactions account for 35−42% of the Hirshfeld surface area in **1a**, **3** and **4a**. On the other hand for **2** it is as low as 17.3%, where the packing is mainly governed by

π···π interactions, and the contribution of C···C contacts is significantly higher compared to the other compounds. The S···H contacts vary significantly, from 8% in **3** to 17.4% in **2**.

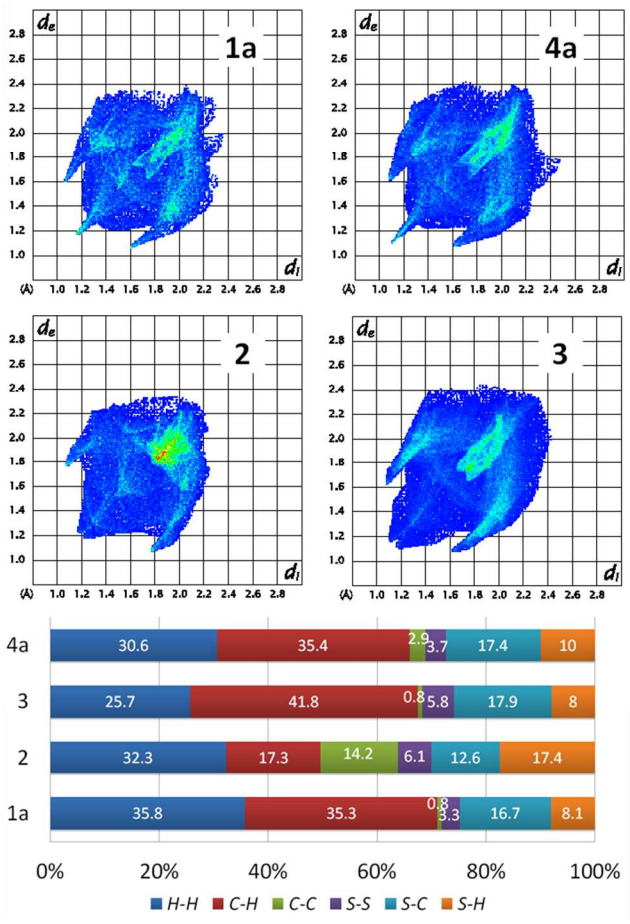

Fig 5. Fingerprint plots (top panels) and relative contributions to the Hirshfeld surface areas for the various intermolecular contacts (bottom panel) for compounds **1a**, **2**, **3** and **4a**.

Electronic structure characterization

The HOMO and lowest unoccupied molecular orbital (LUMO) energies and optical band gaps (E_g) of thin films of **4a,b** were investigated using photoelectron spectrometry in air (PESA) and UV-vis spectroscopy, as collected in Table 2. UV-Vis and PESA spectra are available in supporting information. The electronic structures of **1a** (i.e. monomer of **4a**) were also measured, and the data of **1b** (i.e. octyl-substituted **1a**) were taken from literature for comparison. The absorption edge wavelength (λ_{edge}) of thin films of **1a**, **4a**, and **4b** were shifted to longer wavelengths compared to the solutions (see Figures S14 and S15). Such bathochromic shifts were reported for **1b** (see Table 2) and other conjugated molecules.[23,24] When going from solutions to thin films, the molecular conformation change can lead to a shift in wavelength (e.g. a bathochromic shift in the case of a planarization of backbone), and intermolecular interactions can result in a bathochromic or hypsochromic shift depending on the molecular packing.[24, 25]

Dimerization of **1a** leads to a bathochromic shift and a raised HOMO level in **4a**. The λ_{edge} of thin film of **4a** (420 nm) is larger than that of **1a** (358 nm). The HOMO level in thin film of **4a** (-5.41 eV) is higher than for **1a** (-5.64 eV). The more extended conjugation of **4a** compared to **1a** can explain the larger λ_{edge} and the raised HOMO level of **4a**. The relationship between oligomerization and molecular orbital change agrees well with expected trends as reported in the literature.[24, 26]

Compound **4b** (i.e. alkyl-substituted **4a**) shows HOMO and LUMO levels higher in energy by 0.18 eV and 0.14 eV, respectively, compared to **4a** without significant change in E_g. Alkyl chain are weak electron donating group and usually leads to a small change in energy levels.[27-29] However, **4b** showed a relatively large increase in the HOMO and LUMO levels versus **4a**. Takimiya et al.[30] has observed that the HOMO and LUMO energy levels increase by about 0.5 eV going from non-alkylated molecules to alkyl-substituted ones in thin films, but not in solutions. They suggested that the large energy level increase in thin films may be caused by alkyl chains which promote well-ordered thin films and hence strong intermolecular interactions,[31] which may be the origin of the shift in HOMO and LUMO levels of the alkyl-substituted molecule **4b** compared to **4a**.

The deep HOMO levels of both **4a,b** are desirable for good air stability (HOMO level < -5.2eV).[32, 33] The HOMO level of **4b** (-5.23eV) matches more to the work function of gold (5.2eV)[34] than the one of **4a** (-5.41eV). When the HOMO level of a semiconductor matches well to the work function of electrodes, efficient charge injection is generally obtained if second-order effects, such as interfacial dipole effects, are ignored.[34, 35]

Table 2. Summary of the molecular orbital energies and optical absorption energies of **1a,b** and **4a,b**

Compound	Solution	Thin-film			
	λ_{edge} [nm]	λ_{edge} [nm]	E_g [eV][a]	HOMO [eV][b]	LUMO [eV][c]
1a	340[36]	358	3.46	-5.64	-2.18
1b	354[30, d]	376[30, d]	3.3[30]	-5.3[30]	-2.0[30]
4a	392	420	2.95	-5.41	-2.46
4b	397	426	2.91	-5.23	-2.32

[a)] Estimated from λ_{edge}. [b)] Measured using photoelectron spectrometer in air (PESA). [c)] LUMO = HOMO + E_g. [d)] Calculated using E_g.

Thin-film transistor (TFT) characterization

Thermally evaporated thin-films of **4a,b** were used for TFT characterization. We used a F4-TCNQ charge injection layer in order to reduce the contact resistance in our relatively short channel transistors (L = 50 μm).[37-40] During thin-film deposition, different substrate temperatures (T_{dep}) were used for each batch. We tested three kinds of gate dielectrics: 300 nm SiO_2, 50 nm divinylsiloxane-bis-benzocyclobutene (BCB) on 300 nm SiO_2,[41] and octadecyltrimethoxysilane (OTS)-treated 300 nm SiO_2.

Transistor measurement results for the three gate dielectrics are summarized in Table S1. The saturation-regime mobilities (μ_{sat}) of **4b** were higher than those of **4a** for all the three kinds of dielectrics. Among the three dielectrics, OTS-treated SiO_2 dielectrics led to the highest μ_{sat} values for both compounds (the

data of TFT samples with OTS-treated SiO_2 are shown in Table 3). The averaged μ_{sat} was the highest at T_{dep}=120 °C and 60°C for **4a** and **4b**, respectively, on OTS-treated SiO_2 gate dielectric. The lower T_{dep} of **4b** in the best condition compared to **4a** is beneficial when utilizing flexible plastic substrates.[42] Thin films of both compounds cracked at high T_{dep} only on OTS-treated SiO_2 dielectrics. Increasing T_{dep} to 120°C and 90 °C resulted in cracks for **4a** and **4b**, respectively. At higher T_{dep} the magnitude of the crack formation became larger. On the other two kinds of dielectrics (300 nm SiO_2 and 50 nm BCB on 300 nm SiO_2), there was no crack formation at all investigated T_{dep}. The cracks, only observed on OTS-treated SiO_2 dielectrics, are assumed to result from the high-crystallinity of thin-films grown on top of OTS self-assembled monolayer,[43] and thermal coefficient mismatch between the organic semiconductors and the dielectric.[44, 45] We observed that, for all the three dielectrics and all the tested T_{dep}, mobilities showed an overall increasing trend, as T_{dep} increased, until the thin films cracked.

Table 3. Summary of the TFT performances of **4a,b** prepared using OTS-treated SiO_2 (300 nm) gate dielectric.

Compound	T_{dep} [°C]	μ_{sat} [$cm^2V^{-1}s^{-1}$]	I_{on}/I_{off}	V_T [V]
4a	25	0.09 ± 0.01	(1.5 ± 3.6) × 10^7	-(21 ± 1)
	60	0.39 ± 0.01	(3.7 ± 3.3) × 10^7	-(14 ± 2)
	90	0.41 ± 0.05	(3.6 ± 2.8) × 10^6	-(10 ± 2)
	120	0.67 ± 0.12	(2.9 ± 0.8) × 10^5	-(23 ± 3)
4b	25	0.34 ± 0.04	(2.9 ± 1.2) × 10^5	-(33 ± 1)
	60	1.33 ± 0.09	(7.9 ± 3.1) × 10^5	-(25 ± 1)
	90	1.17 ± 0.09	(1.4 ± 3.2) × 10^6	-(29 ± 1)
	120	0.15 ± 0.02	(1.5 ± 1.2) × 10^6	-(17 ± 3)

Representative saturation transfer curves and output curves of TFTs prepared from **4a,b** are presented in Fig. 6. TFTs of both compounds showed typical current modulation characteristics.[46] The trap densities of **4a** (on OTS-treated SiO_2 and for T_{dep}=120°C) and **4b** (on OTS-treated SiO_2 and for T_{dep}=60°C) estimated from subthreshold swing[47] were (2.9±0.2)×10^{12} and (3.1±0.3)×10^{12} $cm^{-2}eV^{-1}$, respectively. These trap densities were comparable to other organic TFTs[48, 49] and a-Si TFT.[50]

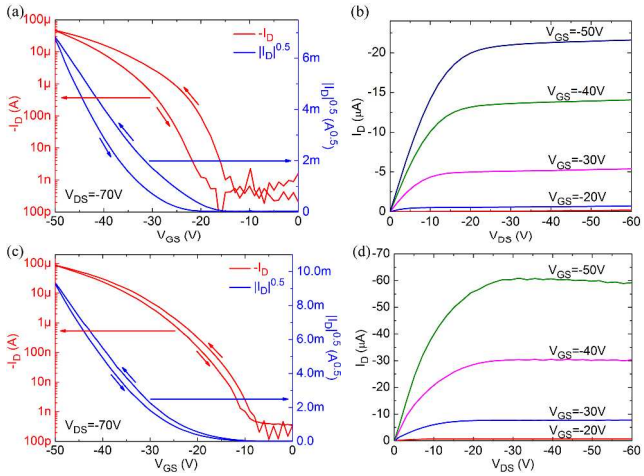

Fig. 6. Representative I-V characteristics of TFTs. The gate dielectric of the TFTs was OTS-treated SiO_2 (300 nm). (a) Bidirectional transfer curves in saturation regime and (b) output curves for a TFT prepared from compound **4a**. (c) Bidirectional transfer curves in saturation regime and (d) output curves for a TFT prepared from compound **4b**.

AFM analysis of thin-films

The surfaces of the thin-films were characterized using atomic force microscopy (AFM). For both **4a** and **4b**, the morphologies of thin films were similar on the three investigated gate dielectrics (see Figures S18 and S19). Figure 7 shows thin films of **4a,b** with a nominal thickness of 40 nm, deposited on OTS-treated SiO_2 (300 nm) at various T_{dep}. Thin films of both compounds exhibited terraced mounds (step height ≈ one molecular length) at the bottom and branched needle-like structures (height of 10-200nm) on top of it. The coexistence of two distinct morphologies was observed in thin films of molecules with herringbone crystal structures.[51, 52] The distances between terrace edges as well as the distances between needle-like structures became longer as we increased T_{dep} for both compounds.

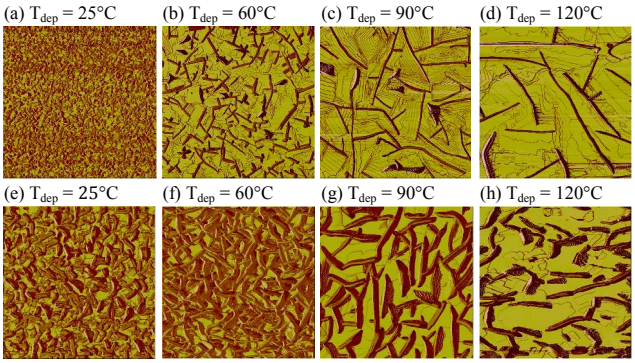

Fig. 7. AFM phase images of thin films of **4a** (a-d) and **4b** (e-h) for various T_{dep}. All thin films (40 nm nominal thickness) were grown on OTS-treated SiO_2 dielectrics. (a-d) are 5μm × 5μm images. (e-h) are 2μm × 2μm images.

In order to elucidate the cluster growth process, the growth of thin films was compared between **4a** and **4b** by obtaining the AFM images of thin films with nominal thicknesses of 1, 3, 6, 10, and 40 nm for T_{dep}=60 °C (see Figures S20 and S21). For both **4a** and **4b**, thin films initially grow in a layer-by-layer fashion. After the first 4-5 and 1-2 layers of **4a** and **4b**, respectively, needle-like structures started to grow in some regions. In a recently reported paper about **4a**,[17] the AFM height images of thin films show only terraced mounds. On the other hand, our thin films of **4a** possess an additional morphology, i.e. needle-like clusters. Even after needle-like structures emerged, terraced mounds still grew layer by layer.

Step heights of terraces and thicknesses of thin films were measured using AFM. The step heights of each terrace of **4a** and **4b** were measured to be 2.2±0.1 nm and 3.9±0.3 nm, respectively. For 40 nm-nominal-thickness films, the thicknesses of the 2D layers (the distances from the dielectric interface to the crevices separating mounds) were 17.8±3.2 nm and 18.9±2.9 nm for **4a** and **4b**, respectively, and were almost constant for all T_{dep}. On average, these thicknesses corresponded to 8.2 layers and 4.8 layers of **4a** and **4b**, respectively. Conducting channels are known

to form principally within the first two monolayers from the dielectric-semiconductor interface in pentacene[53, 54] and sexithienyl.[55] Assuming that this also applies to our molecules, charge transport is expected to occur mainly in the 2D layers (i.e. terraced mounds) of **4a** and **4b**, but slightly in the needle-like structures.

Thin-film X-ray diffraction

Crystal structures of thin films (40nm) of **4a** and **4b** were analyzed using grazing incidence X-ray diffraction (GIXD). Unit cell lattice constants were obtained and are shown in Table S2. The lattice constants of thin films of **4a** were different from those of single crystals of **4a** presented in Table 1. The length of the c axis of **4a** thin film corresponded to that of the long axis of one molecule, whereas in the single crystal unit cell, the c axis had a double molecular length, indicating the possible existence of thin film phase of **4a**. The two sets of lattice constants obtained from single crystals and thin films of **4a** in our work were different from those of phase A and phase A* of **4a** reported by Yu et al[17] (see Table 1 and Table S2). However, it was inconclusive from the data available whether our phase of **4a** thin film was different from the phase A.

When calculating the lattice constants of **4a** and **4b**, a few diffraction peaks (indicated by orange arrows in Figure S23) could not be fitted using the same unit cell, and they also exhibited different full width at half maximum (FWHM), confirming that they did not belong to the same crystalline phase. In order to illuminate the origin of these peaks, we compared GIXD data of 1nm (without needle-like structures) and 6nm thin films (with needle-like clusters) of **4a** and **4b** (their AFM images are given in Figures S20 and S21). Those additional diffraction peaks were not observed in 1nm thin film, but they appeared in the 6nm thin film. This indicated that the additional diffraction peaks can be ascribed to the needle-like clusters, which could be a different crystalline phase of the same material[51, 52, 56] or impurities.[57, 58] Besides the peaks possibly originated by needle-like clusters, **4b** thin film at T_{dep}=120°C showed an additional sets of diffraction peaks which can be due to polymorphism.[59-61]

The interlayer spacings along the (001) direction, d(001), of **4a** and **4b** (2.33nm and 4.03nm, respectively, as shown in Table S2) calculated from x-ray diffraction were in good agreement with the step heights of each terrace of **4a** and **4b** measured using AFM (2.2±0.1 nm and 3.9±0.3 nm, respectively).

Coherence lengths along (110) direction of thin films (40nm) were calculated from full width at half maximum (FWHM) of GIXD peaks (see Figure S24) using Scherrer's equation.[62] As the T_{dep} rose, the coherence lengths of thin films of **4a** and **4b** increased. The coherence lengths of thin films of **4a** and **4b** were comparable with each other, implying similar crystallite size or extent of lattice disorder for both the molecules.[62, 63]

Quantum-chemical calculations and Kinetic Monte Carlo simulations

When comparing the experimental data, the strategy consisting in bridging two BTBT units (**1a** versus **4a**) appears to be slightly less efficient than fusing the units (**1a** versus **3**). In order to shed light at the microscopic level on the charge transport properties, we have first computed for the three derivatives two key parameters at a quantum-chemical level, namely the transfer integrals and the internal reorganization energies[64], see Experimental Section. In a second stage, we have assessed the impact of these molecular parameters on the hole mobility by assuming in first approximation that the transport takes place in a pure hopping regime. To do so, we have injected the molecular parameters in a Marcus-Levich-Jortner expression for the hopping rates, which in turn are used as inputs of Kinetic Monte Carlo simulations to evaluate the hole mobilities from the crystalline structures of the three compounds. As expected from earlier works[65], the internal reorganization energy associated to the positive polaron is decreasing with an increase in the size of the conjugated backbone; it amounts to 225 meV, 123 meV, and 196 meV for **1a**, **3**, and **4a**, respectively. While this decrease is significant going from **1a** to **3**, it is rather limited going from **1a** to **4a** due to the presence of a twist angle between the monomer units. A significant fraction of the reorganization energy in **4a** originates from the fact that the charged compound will tend to get more planar compared to the neutral molecule (from 37° to 26°). The HOMO transfer integrals governing hole transport are displayed in Figure 8. Compound **3** exhibits larger transfer integrals than **1a** and **4a** along the two main transport directions, thus suggesting better hole transport properties. Interestingly, the relative amplitudes of the HOMO transfer integrals along different directions in a layer of the crystalline structure of **1a**, **3**, and **4a** are very similar; *i.e.*, they are large in the short axis direction, intermediate in the diagonal direction and negligible along the long axis direction.

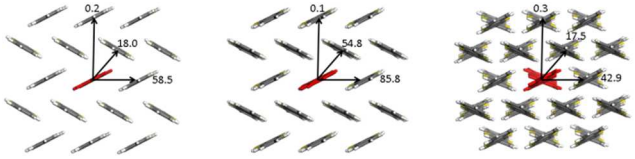

Fig. 8. Representation of the herringbone packing of **1a** (left), **3** (center), and **4a** (right) as well as amplitude of the HOMO transfer integrals (in meV). The short crystalline axis direction corresponds in each case to the horizontal direction.

The anisotropy plots of the hole mobility in a layer of the three crystalline structures are displayed in Figure 9. **3** has the largest hole mobilities, as a result of a smaller reorganization energy and larger transfer integrals. **1a** and **4a** have similar hole transport abilities since the smaller reorganization of **4a**, favorable for charge transport, is compensated by smaller transfer integrals with respect to **1a**. These calculations show that, to make the strategy of bridging monomer units as competitive as fusing the units require to choose monomers that give rise to planar oligomers. For instance, replacing the carbon atoms in the alpha position of the carbon atoms connecting the monomers by nitrogen atoms, which do not bear any hydrogen atom and therefore allow for planarization, could be an interesting derivatization scheme, as far as crystal packing, polymorphism, and charge injection efficiency are not dramatically modified by

this substitution[66].

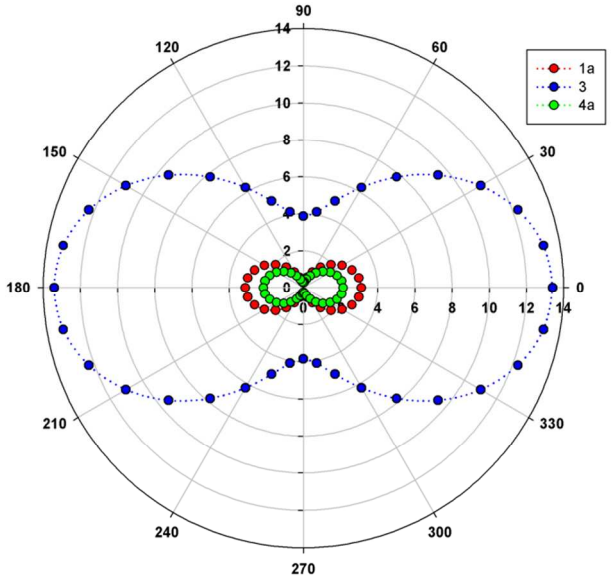

Fig 9. Anisotropy of the hole mobilities (in $cm^2\ V^{-1}\ s^{-1}$) in **1a**, **3**, and **4a**. In each case, the horizontal direction corresponds to the short axis of the crystal.

Conclusions

In conclusion, we successfully synthesized two thienoacene dimers based on the thieno[3,2-*b*]thiophene. The two synthetic pathways developed for the production of the dimers **4a,b** are easily adaptable to scale up for the production of larger amounts of materials. Dimers **4a** and **4b** presented high performances as active hole-transporting thin layer in field-effect transistors, with averaged μ_{sat} of 0.67 and 1.33 $cm^2V^{-1}s^{-1}$, respectively. The dialkyl side chains on **4b** helped to improve its electronic properties as compared to **4a**. However, the dimerization of two BTBT units, i.e. compounds **4a,b**, appears less efficient than their fusion to obtain high mobility values. Interestingly, compounds **3** exhibits a mobility value as high as 5 $cm^2\ V^{-1}\ s^{-1}$. These experimental observations have been corroborated by quantum chemical calculations.

Experimental Section

Chemicals and Instrumentation

Unless otherwise noted, all chemicals were purchased from Aldrich or Acros and used without further purification. TLC were performed using aluminium sheet covered by SiO_2 Silica gel $60F_{254}$ (Merck), and column chromatography using Silica gel 60 (particle size 0.063-0.200 mm, Merck). ^{1}H-NMR (300 MHz) and ^{13}C-NMR (75 MHz) were recorded on Bruker Avance 300. Chemical shifts are given in ppm and coupling constants *J* in Hz. The residual signal of the solvent was taken as internal reference standard. EI-HRMS measurements were made on a Waters AutoSpec 6 and MALDI-ToF experiments on a Waters QToF Premier. [1]benzothieno[3,2-*b*]benzothiophene (**1**),[11] 2-nitro-[1]benzothieno[3,2-*b*]benzothiophene (**5**),[4a] and 2-amino-[1]benzothieno[3,2-*b*]benzothiophene (**6**)[4a] were prepared following literature procedure.

Synthetic Procedure

2-Bromo-[1]benzothieno[3,2-*b*][1]benzothiophene (7): A solution of 2-amino-[1]benzothieno[3,2-*b*][1]benzothiophene (**6**) (4 g, 15.6 mmol) in DMSO (150 mL) at 35 °C was treated with copper(I) bromide (3.36 g, 23.0 mmol) and potassium nitrite (5.33 g, 62.6 mmol). A solution of 48% HBr (7.14 mL, 62.6 mmol) was added dropwise over 2 h, and the mixture stirred 2 h. The mixture was cooled to room temperature, water 100 mL was added, and then filtrated. The precipitate was washed with aqueous ammonia, water, and the MeOH. The residue was dissolved in boiling $CHCl_3$, and filtrated on a silica pad. The resulting residue was subjected to column chromatography [silica, hot *n*-hexane] to afford after crystallization in heptane a white solid (1.69 g, 34%). R_f (*n*-hexane): 0.38; mp: 218 °C; ^{1}H NMR ($CDCl_3$, 25°C) δ: 8.04 (1H, d, J = 1.7 Hz), 7.95 – 7.81 (2H, m), 7.71 (1H, d, J = 8.5 Hz), 7.54 (1H, dd, J = 8.5 and 1.7 Hz), 7.58 – 7.35 (2H, m); ^{13}C NMR ($CDCl_3$, 25°C) δ: 143.6, 142.3, 133.8, 132.9, 132.8, 131.9, 128.3, 126.5, 125.3, 125.0, 124.0, 122.5, 121.6, 118.5; EI-HRMS (C14H7BrS2): [M^+]: calcd 317.9172, found 317.9163.

[1]-Benzothieno[3,2-*b*]-[1]-benzothiophene-2-octan-1-one (8): To a solution of benzothienothiophene **1a** (5.00 g, 20.80 mmol) in dry CH_2Cl_2 (500 mL) was added $AlCl_3$ (9.99 g, 74.89 mmol) in one portion, at -20°C and under an argon atmosphere. The reaction mixture was cooled down to -78°C. Octanoyl chloride (14.20 mL, 83.21 mmol) was then added dropwise in about 20 min. The reaction mixture was stirred further at -78°C for 4h. The reaction was quenched by the addition of ice/water (100 mL). Volatiles were removed under reduced pressure, and the residue was diluted with MeOH (100 mL). The formed precipitate was isolated by filtration, washed with water (3x50 mL) and methanol (3x50 mL) and finally dried to afford **5** (7.04 g, 19.20 mmol, 92 %) as a white powder. This product was used in the next step without additional purification. R_f (*n*-hexane/toluene 2/1 v/v): 0.22; mp: 177-180°C; ^{1}H NMR ($CDCl_3$, 25°C) δ: 8.53 (1H, s, H^1), 8.03 (1H, d, J = 8.3 Hz, H^3), 7.98 – 7.83 (3H, m, H^4, H^6, H^9), 7.54 – 7.39 (2H, m, H^7, H^8), 3.05 (2H, t, J = 7.2 Hz, -CO-CH_2-CH_2-), 1.87 – 1.70 (2H, m, -CO-CH_2-CH_2-), 1.49 – 1.21 (8H, m, -(CH_2)$_4$-CH_3), 0.96 – 0.83 (3H, m, -CH_3); ^{13}C NMR ($CDCl_3$, 25°C) δ: 199.72, 142.94, 142.38, 137.07, 136.38, 133.79, 133.11, 132.91, 125.97, 125.27, 124.85, 124.68, 124.29, 122.21, 121.52, 38.97, 31.89, 29.54, 29.33, 24.70, 22.80, 14.26.

2-Octylbenzo[*b*]benzo[4,5]thieno[2,3-*d*]thiophene (9): To a suspension of ketone **8** (10.00 g, 27.28 mmol) and freshly pulverized KOH (7.64 g, 136.41 mmol) in diethylene glycol (400 ml) was added hydrazine monohydrate (16.54 mL, 341.03 mmol) at room temperature. The reaction mixture was heated to 190-200°C, and stirred at this temperature for 70h. It was then cooled down to room temperature before being poured into methanol (300 mL). The formed precipitate was isolated by filtration and washed with water (3x50 mL) and methanol (3x50 mL). The crude product obtained after drying was purified by column

chromatography on silica gel (eluant: *n*-hexane) to afford **6** (8.50 g, 24.11 mmol, 88%) as white crystals. R_f (*n*-hexane): 0.53; mp: 113-115°C; ^{1}H NMR ($CDCl_3$, 25°C) δ: 7.91 (1H, d, J = 7.7 Hz, H^6), 7.87 (1H, d, J = 8.1 Hz, H^9), 7.79 (1H, d, J = 8.1 Hz, H^4), 7.72 (1H, s, H^1), 7.50 – 7.34 (2H, m, H^7, H^8), 7.28 (1H, d, J = 8.0 Hz, H^3), 2.76 (2H, t, J = 7.6 Hz, Ar-CH_2-CH$_2$-), 1.78 – 1.62 (2H, m, Ar-CH$_2$-CH_2-), 1.44 – 1.19 (10H, m, -(CH_2)$_5$-CH$_3$), 0.95 – 0.82 (3H, m, -CH_3); ^{13}C NMR ($CDCl_3$, 25°C) δ: 142.72, 142.22, 140.54, 133.53, 133.41, 132.73, 131.16, 126.05, 124.95, 124.84, 124.13, 123.50, 121.55, 121.40, 36.30, 32.04, 31.86, 29.65, 29.48, 29.42, 22.83, 14.27; EI-HRMS ($C_{22}H_{24}S_2$): [M^{+}]: calcd 352.1319, found 352.1318.

2-Bromo-7-octyl-[1]benzothieno[3,2-*b*][1]benzothiophene (10): To a solution of monoalkyl **9** (3.00 g, 8.51 mmol) in dry $CHCl_3$ (120 ml) was added dropwise a solution of bromine (1.50 g, 9.39 mmol) in $CHCl_3$ (20 mL), at 0°C, under an argon atmosphere. The reaction mixture was stirred for 20h at 0°C. The reaction was then quenched by the addition of a saturated aqueous solution of $NaHSO_3$ (100 mL). The mixture was extracted with chloroforme (2x100 ml). The combined organic layers were washed with water (100 mL) and brine (100 mL), dried over $MgSO_4$ and concentrated under reduced pressure. The crude product obtained was purified by recrystallization in *n*-hexane, to afford **7** (2.24 g, 5.19 mmol, 61%) as a white solid. R_f (*n*-hexane): 0.60; mp: 188-193°C; ^{1}H NMR ($CDCl_3$, 25°C) δ: 8.03 (1H, d, J = 1.7 Hz, H^1), 7.76 (1H, d, J = 8.1 Hz, H^9), 7.71 (1H, s, H^6), 7.69 (1H, d, J = 8.3 Hz, H^4), 7.54 (1H, dd, J = 8.5, 1.7 Hz, H^3), 7.28 (1H, dd, J = 8.2, 1.4 Hz, H^8), 2.76 (2H, t, J = 7.7 Hz, Ar-CH_2-CH$_2$-), 1.76 – 1.63 (2H, m, Ar-CH$_2$-CH_2-), 1.42 – 1.21 (10H, m, -(CH_2)$_5$-CH$_3$), 0.89 (3H, t, J = 6.7 Hz, -CH_3); ^{13}C NMR ($CDCl_3$, 25°C) δ: 143.63, 142.80, 140.92, 133.89, 132.23, 132.21, 130.88, 128.33, 126.59, 126.22, 123.51, 122.48, 121.42, 118.34, 36.30, 32.04, 31.81, 29.64, 29.46, 29.41, 22.82, 14.26; EI-HRMS ($C_{22}H_{23}BrS_2$): [M^{+}]: calcd 430.0425, found 430.0443.

2,2'-Bi[1]benzothieno[3,2-*b*][1]benzothiophene (4a): In a glove box, a mixture of Ni(COD)$_2$ (596 mg, 2.16 mmol), 1,5-cyclooctadiene (266 µL, 2.16 mmol), and 2,2'-bipyridine (338 mg, 2.16 mmol) was stirred for 15 min in anhydrous DMA (40 mL) in a Schlenk tube, and then **9** (532 mg, 1.66 mmol) was added in one portion. The Schlenk tube was sealed and taken out of the glove box. The mixture was heated at 140 °C overnight. The reaction mixture was allowed to cool to room temperature and poured in aqueous HCl 1M (100 mL). The formed precipitate was isolated by filtration. The solid was washed successively with aqueous HCl 1M (40 mL), water (100 mL), MeOH (50 mL), AcOEt (50 mL), and then diethylether (50 mL). After drying, the crude solid was sublimed twice under vacuum at 320 °C to afford a pale yellow solid **8** (210 mg, 53 %). mp > 300°C; EI-HRMS ($C_{28}H_{14}S_4$): [M^{+}]: calcd 477.9978, found 477.9958.

7,7'-Dioctyl-2,2'-Bi[1]benzothieno[3,2-*b*][1]benzothiophene (4b): In a glove box, a solution of Ni(COD)$_2$ (0.70 g, 2.54 mmol), 1,5-cyclooctadiene (0.31 mL, 2.54 mmol) and bipyridine (0.40 g, 2.54 mmol) in dry toluene (40 mL) was prepared in a Schlenk tube. The reaction mixture was stirred at room temperature for 15 min before the addition of **10** (1.00 g, 2.32 mmol) in one portion. The Schlenk tube was then sealed and taken out of the glove box. The reaction mixture was heated to 80°C and stirred at this temperature overnight. It was then cooled to room temperature before being poured into an equivolumic mixture of methanol and aqueous HCl 1M (200 mL). The formed precipitate was isolated by filtration and washed with aqueous HCl 1M (3*20 mL) and methanol (3*20 mL). The crude solid obtained was purified by recrystallization in chlorobenzene, involving a hot filtration through a pad of celite to get rid of the remaining catalyst traces. **9** (0.53 g, 0.75 mmol, 65 %) was so isolated as a beige solid. mp > 300°C; ^{1}H NMR ($C_2D_2Cl_4$, 100°C) δ: 8.26 (2H, d, J = 1.2 Hz, H^1, $H^{1'}$), 8.00 (2H, d, J = 8.3 Hz, H^4, $H^{4'}$), 7.86 (2H, d, J = 8.5 Hz, H^9, $H^{9'}$), 7.84 (2H, dd, J = 8.3, 1.6 Hz, H^3, $H^{3'}$), 7.80 (2H, s, H^6, $H^{6'}$), 7.36 (2H, dd, J = 8.2, 1.3 Hz, H^8, $H^{8'}$), 2.85 (4H, t, J = 7.7 Hz, Ar-CH_2-CH$_2$-), 1.84 – 1.75 (4H, m, Ar-CH$_2$-CH_2-), 1.52 – 1.32 (20H, m, -(CH_2)$_5$-CH$_3$), 0.99 – 0.93 (6H, m, -CH_3); MALDI-HRMS ($C_{44}H_{46}S_4$): [M^{+}]: calcd 702.2482, found 702.2489.

Single-Crystal X-ray Diffraction

Single-Crystal data collection was carried out with Oxford Diffraction Gemini S diffractometer using MoKα radiation (λ = 1.5418 Å). The crystal structure was solved by direct methods using SHELXS[67] and refined by full matrix least-squares methods based on F^2 using SHELXL97. The displacement parameters of all non-H-atoms were treated anisotropically. H-atoms were placed at calculated positions using suitable riding models with fixed isotropic thermal parameters [U_{iso}(H)=1.2U_{eqv}(C) for CH groups and U_{iso}(H)= 1.5U_{eqv}(C) for CH_3]. Crystal data for **1a** and **4a** are summarized in Table 1.

Hirshfeld Surface Analysis

Hirshfeld Surfaces[68, 69] and the associated fingerprint plots[70] were calculated using Crystal Explorer[71], which accepts a structure input file in the CIF format. Bond lengths to hydrogen atoms were set to typical neutron values (C-H=1.083Å). For each point on the Hirshfeld isosurface, two distances d_e, the distance from the point to the nearest nucleus external to the surface, and d_i, the distance to the nearest nucleus internal to the surface, are defined. The normalized contact distance (d_{norm}) based on d_e and d_i is given by

$$d_{norm} = \frac{(d_i - r_i^{vdW})}{r_i^{vdW}} + \frac{(d_e - r_e^{vdW})}{r_e^{vdW}}$$

where r_i^{vdW} and r_e^{vdW} are the van der Waals radii of the atoms. The value of d_{norm} is negative or positive depending if the intermolecular contacts are shorter or longer than the van der Waals separations. The parameter d_{norm} displays a surface with a red-white-blue color scheme, where bright red spots highlight shorter contacts, white areas represent contacts around the van der Waals separation, and blue regions are devoid of close contacts.

Electronic band structure characterization

Due to the high desorption rate of **1a** even at T_{sub}=20°C, films of **1a** did not form through thermal evaporation. Instead, we used solution shearing to make thin films of **1a**. The details of shearing set-up were published elsewhere.[72] A 2mg/mL solution of **1a** in

chloroform was prepared. The temperature of a sapphire substrate was fixed at 42°C. A thin film of **1a** was formed on the sapphire substrate at a shearing speed of 0.2mm/s, and its optical micrographs are shown in Figure S22. Thin-film samples of **4a,b** were prepared using Angstrom resistive thermal evaporator. We deposited 40 nm-thick films of **4a,b** (nominal thickness, measured by quartz crystal microbalance) on glass substrates under high vacuum (<2×10^{-6}torr) at a rate of 0.1-0.2Å/s. HOMO energy levels were measured by Riken Keiki photoelectron spectrometer in air (PESA, model AC-2) using the thin films. Agilent Cary 6000i UV/Vis/NIR spectrophotometer was utilized to determine the absorption edge (λ_{edge}) and the corresponding optical band gaps (E_g) for the thin films under ambient condition. We obtained the LUMO levels by adding the E_g to the HOMO levels.

TFT fabrication and characterization

TFTs were fabricated with a bottom-gate top-contact configuration. Highly doped (resistivity < 0.005 Ω cm) (100) n-type Si wafers with 300 nm SiO_2 grown by dry thermal oxidation were used as substrates and gate oxides. For BCB (50 nm) on SiO_2 (300 nm) substrate, we used Cyclotene 3022-35 from Dow Chemical Company. Cyclotene solution was diluted using 500 μL Cyclotene and 3 mL mesitylene. After spin-coaing the diluted Cyclotene solution at 3000 rpm for 1 min, the spin-cast thin films were cured at 260 °C for 1 hour in nitrogen. For OTS-treated SiO_2 (300 nm) substrate, we followed the procedure in Bao et al.[73] In order to measure the capacitances of these gate dielectrics, we deposited Au electrodes on top of the gate dielectrics using thermal evaporator. The capacitances were measured by Agilent E4980A Precision LCR Meter and used to calculate the mobility of transistors. For TFT samples, 40 nm-thick (measured using quartz crystal microbalance) films of **4a,b** were deposited on top of the gate dielectrics using Angstrom resistive thermal evaporator under high vacuum (<2×10^{-6} torr) at a rate of 0.1-0.2 Å/s. The substrate temperature was monitored through a thermocouple and controlled during the deposition. After the deposition of **4a,b**, we broke the vacuum and placed shadow masks on top of those organic thin films. Then, a charge injection layer (F_4-TCNQ, 2nm) and source/drain electrodes (Au, 40nm) were deposited consecutively without breaking the vacuum. The channel widths and lengths were 1000 μm and 50 μm, respectively. The transistor characteristics were measured using Keithley 4200-SCS semiconductor parameter analyzer in air under dark condition. We calculated mobilities in the saturation regime (μ_{sat} when V_{DS}=-70V) using the averaged (for the V_{GS} interval of 10V) slopes of $I_D^{1/2}$ vs V_{GS} curves. The V_T values were obtained from an x-intersept of the tangential line at the maximum slope in $I_D^{1/2}$ vs V_{GS} graph. For each condition, 5-10 devices were measured, and averaged values were reported.

AFM and X-ray diffraction analysis of thin-films

We prepared thin-film samples of **4a,b** following the same procedure as that for the samples in electronic band structure characterization. Their substrates were OTS-treated Si wafers with native oxide. Bruker MultiMode System in AFM tapping mode was used to obtain morphological images of the thin films. For grazing incidence X-ray diffraction (GIXD) measurements, we utilized beam line 11-3 (12.73 keV) of Stanford Synchrotron Radiation Lightsource (SSRL) at SLAC National Accelerator Laboratory, Menlo Park, CA, United States,. The incidence angle of X-ray on samples was 0.12°. X-ray diffraction images were saved using 2D image plate (MAR345, 2300×2300 pixels, effective pixel size=150μm). The image plate was placed 400.15mm from the center of samples. The data analysis was performed using the WxDiff software[74] and customized unit cell indexing algorithm.

Quantum-chemical calculations

The hole transport properties of **4a,b**, and **3** have been characterized using the Marcus-Levich-Jortner formalism. This model assumes that charges are hopping between neighboring molecules and that the rate of the hole transfer k_{hop} is given by[64]:

$$k_{hop} = \frac{4\pi^2}{h} J^2 \frac{1}{\sqrt{4\pi\lambda_s k_B T}} \sum_v exp(-S)\frac{S^v}{v!} exp\left[-\frac{(\lambda_s + v\hbar\omega + \Delta G^0)^2}{4\lambda_s k_B T}\right]$$

where S is the Huang-Rhys factor which is related to the internal reorganization energy λ_i ($S = \lambda_i / \hbar\omega$), J the transfer integral, λ_s the external reorganization energy, k_B the Boltzmann constant, T the temperature, ΔG° the free energy of the reaction and ħω an effective vibration mode (carbon-carbon stretching mode) that assists charge transport. The internal reorganization energy entering the Huang-Rhys factor is a parameter that reflects the geometric changes of the molecules involved in the charge transport process upon charge transfer. It has been evaluated at the DFT level (B3LYP/6-31g**) according to the procedure described elsewhere[75]. The ħω effective stretching mode has been set to 0.2 eV and the external reorganization energy to the typical value of 0.1 eV[76]. The HOMO transfer integral (J) describes the amplitude of the interactions between the HOMO electronic levels of the two molecules involved in the hole transfer process. This term has been estimated in a fragment approach at the DFT level (B3LYP/DZ) in the ADF package[77] as described elsewhere[78, 79]. Assuming a weak energetic disorder in crystals, ΔG° can be expressed as $\Delta G° = e\,\vec{F}\,\vec{d}$, where $\vec{F}$ and $\vec{d}$ are the electric field and distance vectors between mass centers, respectively. Finally, the charge carrier mobility (μ) has been obtained using a Kinetic Monte Carlo technique with the First Reaction Method algorithm. This technique allows for the propagation of a single charge carrier in the crystals following a stochastic dynamics where the direction taken by the charge in the crystal after each Monte Carlo cycle is chosen according to the smallest hopping time. The hopping time t_{ij} (rate k_{ij}) between two molecules *i* and *j* is determined using the following expression:

$$t_{ij} = -\frac{ln(r)}{k_{ij}}$$

where *r* is a random number chosen between 0 and 1. The charge carrier mobility is obtained at the end of the simulation as:

$$\mu = \frac{d_{tot}}{t_{tot}F}$$

where d_{tot} and t_{tot} are the total distance travelled during the Kinetic Monte Carlo simulation and the total time of the simulation, respectively.

Acknowledgement

This work has been financially supported by the European Commission / Région Wallonne (FEDER – Smartfilm RF project), the Interuniversity Attraction Pole program of the Belgian Federal Science Policy Office (PAI 7/05), by the Excellence Programme from the Walloon Region (OPTI2MAT project), by a concerted research action of the French Community of Belgian (ARC N° 20061), by the Belgian National Fund for Scientific Research (FNRS - Research fellow PhD grant for GS and project BTBT N°2.4565.11), and by a Marie Curie IIF Scheme of the 7th EU Framework Program for the DISCO-project (N°298319). Y.G. benefits from a mandate of Francqui Research Professor. Y.O. is FNRS Postdoctoral researcher. J.C. is an FNRS Research Director. Y.K. greatly acknowledges the financial support from Kwanjeong Educational Foundation, Republic of Korea.

Notes and references

§ *These two authors have equally contributed and are co-first authors.*
[a] *Université Libre de Bruxelles (ULB), Laboratory of Polymer Chemistry , C.P. 206/01, Boulevard du Triomphe, 1050 Bruxelles, Belgium. Fax: +32 2650 5410; Tel: +32 2650 5390; E-mail: ygeerts@ulb.ac.be*
[b] *Department of Electrical Engineering, Stanford University, Stanford, California, 94305, USA*
[c] *Department of Chemical Engineering, Stanford University, Stanford, California, 94305, USA*
[d] *Service de Chimie des Matériaux Nouveaux, Université de Mons (UMons), Place du Parc 20, 7000 Mons, Belgium*
[e] *Department of Pure and Applied Chemistry, University of Strathclyde, 295 Cathedral Street, Glasgow G1 1XL; Scotland*
[f] *Center for Advancing Electronics Dresden, Technische Universität Dresden, 01062 Dresden, Germany*

† Electronic Supplementary Information (ESI) available: ^{1}H and ^{13}C NMR spectra, mass spectra, absorption and fluorescence, PESA spectra, transistor characteristics, thin-film morphologies, and GIXD of thin films, See DOI: 10.1039/b000000x/

1. J. E. Anthony, *Angew. Chem. Int. Ed.*, 2008, 47, 452-483.
2. J. E. Anthony, *Chem. Rev.*, 2006, 106, 5028-5048.
3. K. Takimiya, S. Shinamura, I. Osaka and E. Miyazaki, *Advanced Materials*, 2011, 23, 4347-4370.
4. C. Wang, H. Dong, W. Hu, Y. Liu and D. Zhu, *Chem. Rev.*, 2011, 112, 2208-2267.
5. J. Huang, H. Luo, L. Wang, Y. Guo, W. Zhang, H. Chen, M. Zhu, Y. Liu and G. Yu, *Org. Lett.*, 2012, 14, 3300-3303.
6. B. Kosata, V. Kozmik and J. Svoboda, *Collect. Czech. Chem. Commun.*, 2002, 67, 645-664.
7. B. Kosata, V. Kozmik, J. Svoboda, V. Novotna, P. Vanek and M. Glogarova, *Liq. Cryst.*, 2003, 30, 603-610.
8. B. Kosata, J. Svoboda, V. Novotna and M. Glogarove, *Liq. Cryst.*, 2004, 31, 1367-1380.
9. C. Lo, A. Adenier, K. I. Chane-Ching, F. Maurel, J. J. Aaron, B. Kosata and J. Svoboda, *Synth. Met.*, 2006, 156, 256-269.
10. C. Ruzié, J. Karpinska, A. R. Kennedy and Y. H. Geerts, *J. Org. Chem.*, 2013, 78, 7741-7748.
11. K. Takimiya, H. Ebata, K. Sakamoto, T. Izawa, T. Otsubo and Y. Kunugi, *J. Am. Chem. Soc.*, 2006, 128, 12604-12605.
12. H. Ebata, T. Izawa, E. Miyazaki, K. Takimiya, M. Ikeda, H. Kuwabara and T. Yui, *J. Am. Chem. Soc.*, 2007, 129, 15732-15733.
13. T. Yamamoto, T. Nishimura, T. Mori, E. Miyazaki, I. Osaka and K. Takimiya, *Org. Lett.*, 2012, 14, 4914-4917.
14. K. Takimiya, M. Nakano, M. J. Kang, E. Miyazaki and I. Osaka, *Eur. J. Org. Chem.*, 2013, 2013, 217-227.
15. T. Mori, T. Nishimura, T. Yamamoto, I. Doi, E. Miyazaki, I. Osaka and K. Takimiya, *J. Am. Chem. Soc.*, 2013, 135, 13900-13913.
16. *Japan Pat.,* JP2009182034A, 2009.
17. H. Yu, W. Li, H. Tian, H. Wang, D. Yan, J. Zhang, Y. Geng and F. Wang, *ACS Appl. Mater. Interfaces*, 2014, 6, 5255-5262.
18. M. Saito, I. Osaka, E. Miyazaki, K. Takimiya, H. Kuwabara and M. Ikeda, *Tetrahedron Lett.*, 2011, 52, 285-288.
19. A. Y. Amin, A. Khassanov, K. Reuter, T. Meyer-Friedrichsen and M. Halik, *J. Am. Chem. Soc.*, 2012, 134, 16548-16550.
20. C. M. Combe, L. Biniek, B. C. Schroeder and I. McCulloch, *J. Mater. Chem. C*, 2014, 2, 538-541.
21. E. Modau, D. C. Liles and P. H. van Rooyen, *Acta Crystallogr. Sect. Sect. E: Struct. Rep. Online*, 2012, 68, o580-o580.
22. C. Grigoriadis, C. Niebel, C. Ruzié, Y. H. Geerts and G. Floudas, *J. Phys. Chem. B*, 2014, 118, 1443-1451.
23. T.-A. Chen, X. Wu and R. D. Rieke, *J. Am. Chem. Soc.*, 1995, 117, 233-244.
24. J. K. Politis, F. B. Somoza, J. W. Kampf, M. D. Curtis, L. González Ronda and D. C. Martin, *Chem. Mater.*, 1999, 11, 2274-2284.
25. F. Cicoira and C. Santato, *Organic Electronics: Emerging Concepts and Technologies*, John Wiley & Sons, 2013.
26. C. Chi and G. Wegner, *Macromol. Rapid Commun.*, 2005, 26, 1532-1537.
27. L. Zhang, L. Tan, Z. Wang, W. Hu and D. Zhu, *Chem. Mater.*, 2009, 21, 1993-1999.
28. A. Facchetti, M.-H. Yoon, C. L. Stern, G. R. Hutchison, M. A. Ratner and T. J. Marks, *J. Am. Chem. Soc.*, 2004, 126, 13480-13501.
29. R. Li, X. Zhang, P. Zhu, D. K. P. Ng, N. Kobayashi and J. Jiang, *Inorg. Chem.*, 2006, 45, 2327-2334.
30. K. Takimiya, I. Osaka, T. Mori and M. Nakano, *Acc. Chem. Res.*, 2014, DOI: 10.1021/ar400282g.
31. H. Inokuchi, G. Saito, K. Seki, P. Wu, T. B. Tang, T. Mori, K. Imaeda, T. Enoki, Y. Higuchi and K. Inaka, *Chem. Lett.*, 1986, 15, 1263-1266.
32. D. M. de Leeuw, M. M. J. Simenon, A. R. Brown and R. E. F. Einerhand, *Synth. Met.*, 1997, 87, 53-59.
33. B. C. Thompson, Y.-G. Kim and J. R. Reynolds, *Macromolecules*, 2005, 38, 5359-5362.
34. S. Braun, W. R. Salaneck and M. Fahlman, *Adv. Mater.*, 2009, 21, 1450-1472.
35. H. Ishii, K. Sugiyama, E. Ito and K. Seki, *Adv. Mater.*, 1999, 11, 605-625.
36. S. Shinamura, E. Miyazaki and K. Takimiya, *J. Org. Chem.*, 2010, 75, 1228-1234.
37. J. Soeda, Y. Hirose, M. Yamagishi, A. Nakao, T. Uemura, K. Nakayama, M. Uno, Y. Nakazawa, K. Takimiya and J. Takeya, *Adv. Mater.*, 2011, 23, 3309-3314.
38. N. Koch, S. Duhm, J. P. Rabe, A. Vollmer and R. L. Johnson, *Phys. Rev. Lett.*, 2005, 95, 237601.
39. N. Koch, *ChemPhysChem*, 2007, 8, 1438-1455.
40. H. Klauk, G. Schmid, W. Radlik, W. Weber, L. Zhou, C. D. Sheraw, J. A. Nichols and T. N. Jackson, *Solid-State Electronics*, 2003, 47, 297-301.
41. L.-L. Chua, J. Zaumseil, J.-F. Chang, E. C. W. Ou, P. K. H. Ho, H. Sirringhaus and R. H. Friend, *Nature*, 2005, 434, 194-199.
42. V. Zardetto, T. M. Brown, A. Reale and A. Di Carlo, *J. Polym. Sci., Part B: Polym. Phys.*, 2011, 49, 638-648.
43. M.-M. Ling, Z. Bao and P. Erk, *Appl. Phys. Lett.*, 2006, 89, -.
44. J. Locklin, D. Li, S. C. B. Mannsfeld, E.-J. Borkent, H. Meng, R. Advincula and Z. Bao, *Chem. Mater.*, 2005, 17, 3366-3374.

45. J. Locklin, M. E. Roberts, S. C. B. Mannsfeld and Z. Bao, *Polymer Reviews*, 2006, 46, 79-101.
46. J. Zaumseil and H. Sirringhaus, *Chem. Rev.*, 2007, 107, 1296-1323.
47. W. L. Kalb and B. Batlogg, *Physical Review B*, 2010, 81, 035327.
48. M. McDowell, I. G. Hill, J. E. McDermott, S. L. Bernasek and J. Schwartz, *Appl. Phys. Lett.*, 2006, 88, -.
49. M.-H. Yoon, C. Kim, A. Facchetti and T. J. Marks, *J. Am. Chem. Soc.*, 2006, 128, 12851-12869.
50. A. Rolland, J. Richard, J. P. Kleider and D. Mencaraglia, *J. Electrochem. Soc.*, 1993, 140, 3679-3683.
51. G. Hlawacek, P. Puschnig, P. Frank, A. Winkler, C. Ambrosch-Draxl and C. Teichert, *Science*, 2008, 321, 108-111.
52. M. Campione, A. Sassella, M. Moret, A. Papagni, S. Trabattoni, R. Resel, O. Lengyel, V. Marcon and G. Raos, *J. Am. Chem. Soc.*, 2006, 128, 13378-13387.
53. B. Park, S. Seo and P. G. Evans, *J. Phys. D: Appl. Phys.*, 2007, 40, 3506.
54. N. Yoneya, M. Noda, N. Hirai, K. Nomoto, M. Wada and J. Kasahara, *Appl. Phys. Lett.*, 2004, 85, 4663-4665.
55. F. Dinelli, M. Murgia, P. Levy, M. Cavallini, F. Biscarini and D. M. de Leeuw, *Phys. Rev. Lett.*, 2004, 92, 116802.
56. H. Plank, R. Resel, H. Sitter, A. Andreev, N. S. Sariciftci, G. Hlawacek, C. Teichert, A. Thierry and B. Lotz, *Thin Solid Films*, 2003, 443, 108-114.
57. E. Gomar-Nadal, B. R. Conrad, W. G. Cullen and E. D. Willams, *J. Phys. Chem. C*, 2008, 112, 5646-5650.
58. B. R. Conrad, E. Gomar-Nadal, W. G. Cullen, A. Pimpinelli, T. L. Einstein and E. D. Williams, *Phys. Rev. B*, 2008, 77, 205328.
59. A. C. Mayer, A. Kazimirov and G. G. Malliaras, *Phys. Rev. Lett.*, 2006, 97, 105503.
60. T. Kakudate, N. Yoshimoto and Y. Saito, *Appl. Phys. Lett.*, 2007, 90, 081903.
61. R. J. Chesterfield, J. C. McKeen, C. R. Newman, P. C. Ewbank, D. A. da Silva Filho, J.-L. Brédas, L. L. Miller, K. R. Mann and C. D. Frisbie, *J. Phys. Chem. B*, 2004, 108, 19281-19292.
62. D.-M. Smilgies, *J. Appl. Crystallogr.*, 2009, 42, 1030-1034.
63. M. Birkholz, *Thin film analysis by X-ray scattering*, John Wiley & Sons, 2006.
64. V. Coropceanu, J. Cornil, D. A. da Silva Filho, Y. Olivier, R. Silbey and J.-L. Brédas, *Chem. Rev.*, 2007, 107, 926-952.
65. V. Coropceanu, M. Malagoli, D. da Silva Filho, N. Gruhn, T. Bill and J. Brédas, *Phys. Rev. Lett.*, 2002, 89, 275503.
66. G. Schweicher, Y. Olivier, V. Lemaur and Y. H. Geerts, *Isr. J. Chem.*, 2014.
67. G. Sheldrick, *Acta Cryst.*, 2008, 64A, 112-122.
68. M. A. Spackman and D. Jayatilaka, *CrystEngComm*, 2009, 11, 19-32.
69. M. A. Spackman, *Phys. Scr.*, 2013, 87, 048103.
70. M. A. Spackman and J. J. McKinnon, *CrystEngComm*, 2002, 4, 378-392.
71. D. J. G. S.K. Wolff, J.J. McKinnon, M.J. Turner, D. Jayatilaka, M.A. Spackman, University of Western Australia, CrystalExplorer (Version 3.1) edn., 2012.
72. G. Giri, E. Verploegen, S. C. B. Mannsfeld, S. Atahan-Evrenk, D. H. Kim, S. Y. Lee, H. A. Becerril, A. Aspuru-Guzik, M. F. Toney and Z. Bao, *Nature*, 2011, 480, 504-508.
73. Y. Ito, A. A. Virkar, S. Mannsfeld, J. H. Oh, M. Toney, J. Locklin and Z. Bao, *J. Am. Chem. Soc.*, 2009, 131, 9396-9404.
74. S. C. B. Mannsfeld, M. L. Tang and Z. Bao, *Adv. Mater.*, 2011, 23, 127-131.
75. V. Lemaur, D. A. da Silva Filho, V. Coropceanu, M. Lehmann, Y. Geerts, J. Piris, M. G. Debije, A. M. van de Craats, K. Senthilkumar, L. D. A. Siebbeles, J. M. Warman, J.-L. Brédas and J. Cornil, *J. Am. Chem. Soc.*, 2004, 126, 3271-3279.
76. N. G. Martinelli, J. Idé, R. S. Sánchez-Carrera, V. Coropceanu, J.-L. Brédas, L. Ducasse, F. Castet, J. Cornil and D. Beljonne, *The Journal of Physical Chemistry C*, 2010, 114, 20678-20685.
77. G. Te Velde, F. M. Bickelhaupt, E. J. Baerends, C. Fonseca Guerra, S. J. van Gisbergen, J. G. Snijders and T. Ziegler, *J. Comput. Chem.*, 2001, 22, 931-967.
78. E. F. Valeev, V. Coropceanu, D. A. da Silva Filho, S. Salman and J.-L. Brédas, *J. Am. Chem. Soc.*, 2006, 128, 9882-9886.
79. L. Viani, Y. Olivier, S. Athanasopoulos, D. A. da Silva Filho, J. Hulliger, J. L. Brédas, J. Gierschner and J. Cornil, *ChemPhysChem*, 2010, 11, 1062-1068.

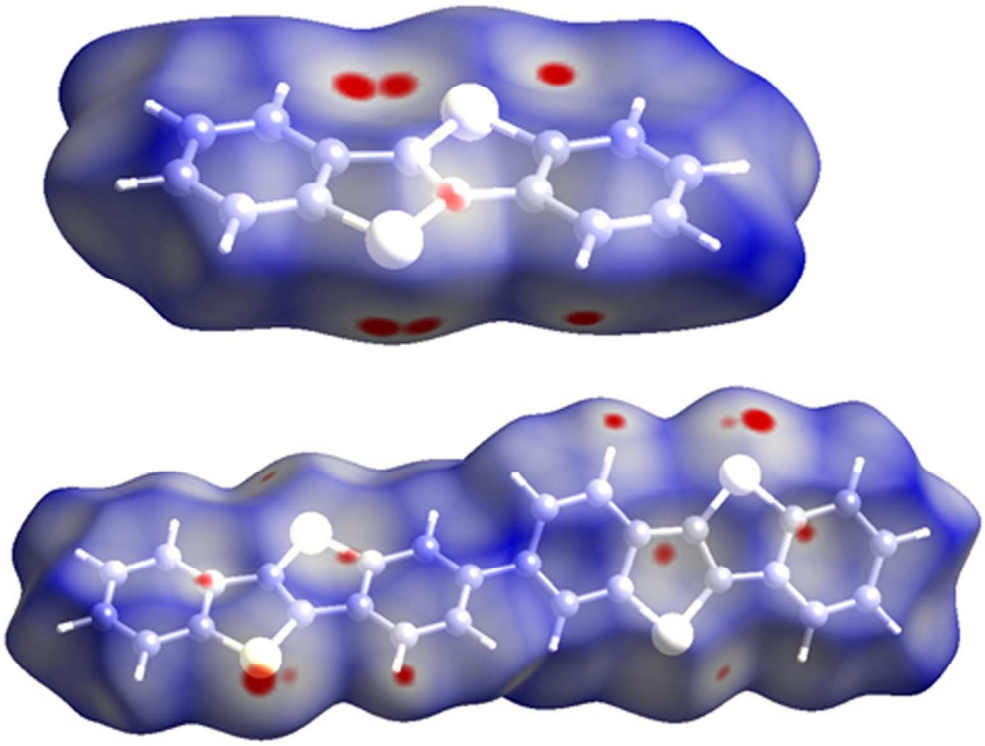

Two thienoacene dimers based on the thieno[3,2-b]thiophene moiety were efficiently synthesized, characterized and evaluated as active hole-transporting layers in organic field-effect transistors.
101x78mm (300 x 300 DPI)